Research Article | Vol. 32, No. 25 / 2 Dec 2024 / Optics Express 43788

Optics EXPRESS

Soft X-ray chemically sensitive ptychographic imaging of 3D nano-objects

VITALY KRASNOV,[1,2,*,†] IGOR MAKHOTKIN,[3,†] JEROEN E. SCHEERDER,[1,†] LARS LOETGERING,[4,5,6,7,†] VICTOR SOLTWISCH,[8,†] PAUL A. W. VAN DER HEIDE,[1,†] AND CLAUDIA FLEISCHMANN[1,2,†]

[1] *imec, Kapeldreef 75, Leuven 3001, Belgium*
[2] *Quantum Solid-State Physics Group, KU Leuven, Celestijnenlaan 200D, Leuven 3001, Belgium*
[3] *Currently with the University of Twente, Drienerlolaan 5, Enschede 7522 NB, Netherlands*
[4] *Institute of Applied Physics, Abbe Center of Photonics, Friedrich-Schiller-University Jena, Albert-Einstein-Straße 15, Jena 07745, Germany*
[5] *Helmholtz-Institute Jena, Fröbelstieg 3, Jena 07743, Germany*
[6] *Helmholtzzentrum für Schwerionenforschung, Planckstraße 1, Darmstadt 64291, Germany*
[7] *Carl Zeiss AG, Carl-Zeiss-Promenade 10, Jena 07745, Germany*
[8] *PTB, Abbestraße 2, Berlin 10587, Germany*
[†] These authors contributed equally
[*] *vitaly.krasnov@imec.be*

Abstract: The results of a soft X-ray chemically sensitive ptychographic imaging of non-planar nanoscale 3D objects - atom probe tomography tips, with resolution down to 12 nm at 800 eV using scanning X-ray microscope at the electron storage ring BESSY II are presented. We validate that this approach can be used to determine the tip (emitter) shape, and to resolve inner nano-scale structures as relevant for semiconductor applications and even for quantitative chemical composition analysis. Imaging of buried interfaces with below 30 nm resolution is demonstrated. This work might pave the way for contactless, ptychographic in-situ characterization of APT tips with tabletop coherent EUV sources.

© 2024 Optica Publishing Group under the terms of the Optica Open Access Publishing Agreement

1. Objectives and motivation

X-ray coherent diffraction imaging (CDI) opens a wide perspective for non-destructive, chemically sensitive in-depth imaging of nano-structures with resolution determined primarily by the wavelength of light and the detector numerical aperture (NA). The paramount benefit of CDI-based techniques over conventional X-ray microscopy is that CDI generally does not rely on complex high-quality X-ray optics. However, in order to obtain a reconstructed image of an object, generally, a large amount of diffraction data, so-called over-sampling, is required. Ptychography is a form of coherent diffractive imaging (CDI) technique in which the sample is scanned with a focused light beam to reach the necessary amount of over-sampled data by recording multiple diffraction patterns (one for each position). The distance between neighboring scan positions is a fraction of the illumination spot size (typically ~60% overlap is required) [1,2]. This allows us to reach the necessary amount of oversampling and enables efficient decoupling of sample and probe functions as well as "stitching" of sample image fragments during the ptychographic reconstruction process. The technique allows for the reconstruction of both amplitude and phase distributions in the sample plane, much like holography, via customized iterative phase retrieval algorithms [3–6]. Utilizing information on both absorption and phase shift in every pixel of the sample's image enables chemical resolution by calculating the so-called scattering quotient [7]. It is derived from the refractive index n and the extinction coefficient k and is calculated from the phase shift and absorption values. One cannot determine n and k values from the

#535314 https://doi.org/10.1364/OE.535314
Journal © 2024 Received 26 Jul 2024; revised 5 Oct 2024; accepted 10 Oct 2024; published 18 Nov 2024

phase shift and the absorption values alone without knowledge of the sample thickness. Yet the scattering quotient can be determined, and as it is unique for each material and wavelength, this allows for chemical identification by comparing experimental values with tabular ones. The large number of collected diffraction patterns provides a tremendous level of data redundancy (i.e. total pixel count in all the diffraction patterns is much higher than the number of pixels in the object), which enables both high resolution and high signal-to-noise ratio. Being contactless and non-destructive, ptychography gained extended popularity for variety of applications in recent years: biological tissues imaging [7–9], structures height profile measurements [10–13], X-ray optics characterization [14], magnetic imaging [15], imaging of thin films [16–20], buried interfaces imaging [21], semiconductor structures imaging [22,23], internal structures imaging [24], and buried defects characterization [25]. Later the technique was adapted for transmission electron microscopy (TEM) as well. Some examples of TEM ptychography include but are not limited to: structural imaging [26], actinic imaging with sub-angstrom resolution [27], crystalline structure imaging [28], and single particle imaging [29].

Given the high spatial resolution that can be achieved with ptychographic CDI, we recently proposed [30] its exploitation to image atom probe samples. Atom probe tomography (APT) is highly complementary to TEM, as it enables nano-scale compositional analysis on 3D objects, which has triggered lots of attention in the semiconductor industry [31,32]. For APT analysis, the samples are shaped into a nano-sized object that resembles a tomography pin [9] but with much tighter aspect ratio and dimensions, i.e. the tip's endpoint has a radius of less than 100 nm, the lengths can be several hundreds to thousands of nanometer while the thickness of the sample changes along its z-axis with typical taper angles around 5 to 10°.

While APT is capable of atom-level resolution, the accuracy and resolution in APT is sample dependent. The reason is, in an atom probe microscope, the sample itself acts as the ion optics and thereby its shape and properties define the magnification during analysis.

During APT analysis, atoms are field evaporated from the tip surface via the effect of a combined electric field (several tens of V/nm) and a short voltage (ns) or laser (ps) pulse. The extracted ions are accelerated towards a position sensitive detector that registers their time-of-flight (i.e. mass-to-charge ratio), as well as their x-y impact position and sequence. Via simple backward projection algorithms [33,34], one reconstructs a 3D point cloud (x-y-z) of the sample volume in which all detected atoms are identified. While the exact ion trajectories will be defined by the shape of the atom probe tip, especially by its end point topography [35–40], current reconstruction algorithms simply assume a hemispherical end shape without any (varying) topology. A simplification that is no longer justified for heterogenous samples and that introduces distortions due to faulty x-y-z positions in the reconstructed volume. To overcome this problem, research efforts are being undertaken to experimentally determine the tip (end) shape. Based on this, realistic ion trajectories can be calculated to avoid oversimplified backward projection, which ultimately paves the way for more accurate reconstruction algorithms which are being developed in the community [41–43]. Motivated by the need for a fast, contactless, and high-resolution tip shape imaging method we set out to evaluate the capabilities of CDI for that purpose.

The main objective of this work was to perform a proof-of-concept study that shall validate the feasibility and the limitations of a ptychographic imaging of atom-probe tomography tips, to determine the best-achievable spatial resolution, required measurement conditions, and chemical sensitivity. On the long-term, such research could contribute to the potential hybridization of a soft X-ray/EUV imaging system with an atom probe microscope, to access structural information about the tip shape in-situ during an APT measurement. This information will allow for the determination of the ion trajectories, and hence the ions' original positions more accurately. Such a system is envisioned as a stepping-stone to improve the spatial accuracy of APT especially in heterogeneous material systems [41,42,44]. As examples have proven, the hybridization of (complex) characterization equipment is not an unfeasible endeavor. For examples, researchers

Optics EXPRESS

at NIST Boulder have integrated a table-top EUV light source into an atom probe microscope [45]. In their system, the EUV light source is utilized to trigger field-evaporation of atoms from the APT sample rather than for imaging purposes. Or at the Ernst-Ruska centre in Germany a combined TEM-APT setup is being built with the purpose to achieve fully correlative, nano-scale materials characterization [46].

So far, most high-resolution EUV / X-ray ptychographic images, for example as reported in [10] were taken from thin film samples with imprints or holes, showing spatial resolution smaller than 10 nm [14]. There are a number of works where soft X-ray CDI was performed on non-actinic structures, for example: tomographic 3D imaging of uniform porous gold nano-structure with ptychography [24]; ptychographic imaging of Allende meteorite grain sample [26]; single-shot CDI tomographic imaging of a yeast cell [47]; tomographic 3D imaging of bone structure with ptychography [9]; single-shot CDI of live cells [48]. In this paper we show the results of soft X-ray ptychographic imaging of APT tips. The shape of a typical APT tip significantly differs from both a typical thin planar sample for which the ptychography resolution is studied, and the more arbitrary 3D samples like grains or cells. The APT tip represents a conical needle with the apex radii ~100 nm, where both the internal and the surface structure of the top few hundred nm is of interest [31]. This is a challenge for CDI since planar approximation of the object is no longer correct, which leads to a decrease of resolution in the lower, and thus thicker part of the tip. On the other hand, the apex of the tip is very small both in lateral and axial dimensions. This leads to a miniscule change in the absorption and phase shift resulting in low contrast and, consequently, also lower resolution, and higher requirements for detector's dynamic range. To test the capability of ptychographic imaging for such samples, we have prepared two realistic test systems, which are highly relevant for semiconductor applications [42,49–52].

System 1 (Fig. 1 left) represents a 230 nm thick SiGe multilayer film stack with thickness of a single layer ~20 nm in which the $Si_{1-x}Ge_x$ concentration gradually varies from the top to the bottom of the sample. The multilayer region is grown on a ~1 μm Ge buffer layer on a silicon substrate. Imaging of this sample allowed us to quantitatively evaluate chemical resolution of the technique. System 2 is comprised of an 80 nm wide Si fin embedded in SiO_2, and was used to evaluate whether the contrast is enough to resolve a nanostructure embedded in such a needle (see Fig. 1 right). In the preparation of these tip specimen, ion beam induced Pt layers were deposited (see section 2), and were left intentionally to take advantage of high contrast provided by Pt in EUV.

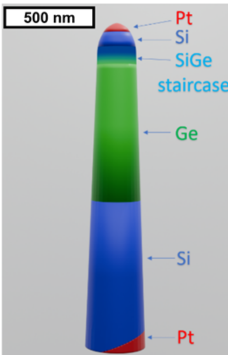

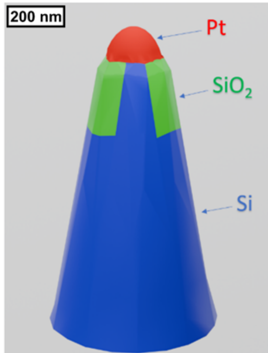

Fig. 1. Schematic models of System 1 (left) and System 2 (right)

Optics EXPRESS

2. Experimental setup

The samples have been imaged using various wavelengths in the range from 1.03 nm (750 eV) to 1.65 nm (1200 eV) on the MAXYMUS beamline at the electron storage ring BESSY II. The image and the scheme of the setup are shown in Fig. 2. A grating and a pair of slits were used to monochromize the beam. SiN Fresnel zone plate (FZP) with the diameter of 120 µm, 60 µm beamstop, and outer zone width of 100 nm had 8 mm focal distance at 800 eV, and in conjunction with order sorting aperture (OSA) focused the soft X-ray beam onto the sample into a 1 µm spot. Since authors did not contribute to the construction of the MAXYMUS endstation, the detailed description of the setup is not given here but can be found instead in [53].

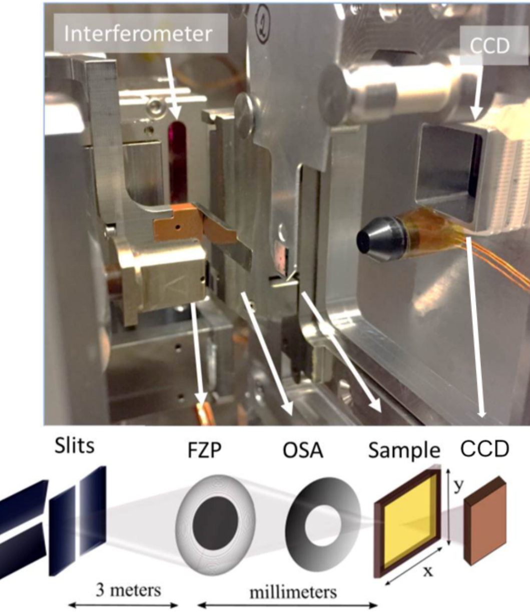

Fig. 2. Experimental setup: FZP – Fresnel zone plate, OSA – order sorting aperture. Image from [53].

To both control position and account for drifts and vibrations, the sample stage is equipped with a differential laser interferometer system which provides position accuracy of 2.5 nm.

Diffraction patterns were registered with a PnCCD X-Ray camera. Its sensor from MPG HLL has 264×264 pixels with 48 µm pixel pitch, < 3e RMS readout noise, and 100 ke full well capacitance. Considering that distance from the sample to the detector was 8.5 cm, the numerical aperture (NA) was equal to 0.075. This results in resolution limit of $\lambda/2$ NA = 11 nm at 800 eV.

For each sample a set of ptychography scans (from 400 to 10 000 diffraction patterns each) with various step sizes (40 to 120 nm) and data-point acquisition times (50 to 2000ms) were measured and analyzed. Number of scan positions is larger, and step size is smaller (only 4-12% of the illumination spot size) than usual [1,54] for ptychography to accommodate for the relatively small number of pixels of the camera sensor.

Examples of typical registered diffraction patterns corresponding to a Siemens star test target, an APT tip (system 1) and the beam without a sample inserted are shown in Fig. 3 (from left to right). Note the lack of diffraction features when the light is being diffracted at the APT tip as compared to the rich pattern observed from diffraction at the Siemens star.

All reconstructions shown in this manuscript were performed in MATLAB using the momentum-accelerated ptychographical iterative engine (mPIE) algorithm [55] implemented in an open-source

Optics EXPRESS

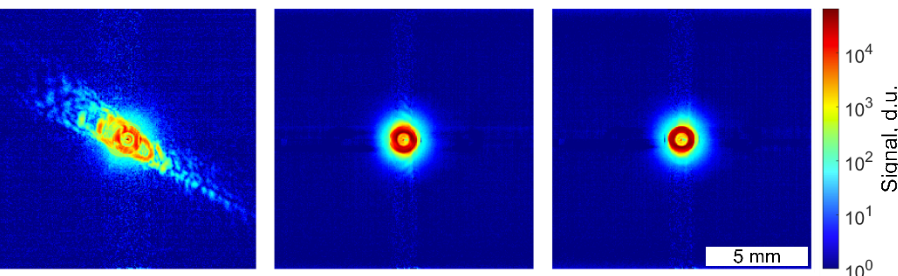

Fig. 3. Examples of the diffraction patterns corresponding to Siemens star test target (left) and SiGe staircase APT tip (center), the beam on the CCD without sample in place (right). All three images share the colorbar indicating intensity in logarithmic scale and the scalebar to the right.

software PtyLab [56]. mPIE is a state-of-the-art ptychographic algorithm which is based on extended ptychographical iterative engine (ePIE) [6] with much higher than ePIE convergence rate. It is described in more detail in Section 5.1.

Atom probe sample preparation

Needle shaped specimens were prepared by employing a standard lift-out and apex sharpening technique [57] using the Helios G3 CX focused ion beam – scanning electron microscope (FIB-SEM) from Thermofisher Scientific. In the first step of the specimen preparation, a protective Pt cap was deposited on the sample surface using either ion- or electron-beam induced deposition with a gas injection system (GIS). A $^{69}Ga^{+}$ beam was used at 30 kV to lift out part of the sample, connect it to a carrier wire using another Pt deposition, and to reach a specimen apex diameter of $\sim$ 100-200 nm. Then, the beam energy was decreased to 5 kV before further shrinking of the tip diameter to reduce beam-induced damage and Ga-implantation in the resulting specimen. For APT specimens, it is customary to fully remove the Pt cap. For the systems reported in this work, part of the Pt cap was not removed, as this layer provides additional contrast in the ptychographic images.

While several tips were imaged with CDI, this manuscript is being restricted to two examples which are presentative for all other measurements and allowed us to evaluate the accuracy on the dimensional measurements in the reconstructed structures, the spatial resolution and chemical sensitivity achieved.

3. Experimental results

3.1. Quantitative chemical mapping

Imaging nanoscale 3D object such as an APT tip represents a challenge since the thickness (i.e. optical path) is different in each point of an image: light propagation distance depends on X and Y coordinates of the scan due to the cone shape of the needle. Without knowing this thickness distribution, it is impossible to determine n and k values from reconstructed phase and amplitude distributions alone. However, there is a way to use these distributions to calculate so-called scattering quotient [7] distribution which is independent of sample thickness and enables accurate determination of chemical elements and composition by comparing experimental values with tabular ones. This technique is described in more detail in Section 5.3.

To estimate the ability of the technique to resolve small changes in a chemical composition, we had performed ptychographic imaging of the APT needle containing a SiGe staircase, consisting of three elements: Si, Ge and Pt, and in which the concentration gradually changes from Si to Ge over a 180 nm thick region.

The quality of reconstruction of the inner buried structure strongly depends on the optical contrast between the materials, i.e. the complex refractive index $n = (1 - \delta) - i \cdot \beta$, where δ is the refractive index decrement, and β is the absorption index. The optical constants for Si and Ge are presented in Fig. 4, demonstrating that the highest contrast can be achieved around the Ge L absorption edge at ∼ 1230 eV due to largest β difference between materials, however, lower δ values for both materials as well as lower β of Si reduce the diffraction efficiency of the tip resulting in lower contrast and signal-to-noise ratio (SNR) in the reconstructed images.

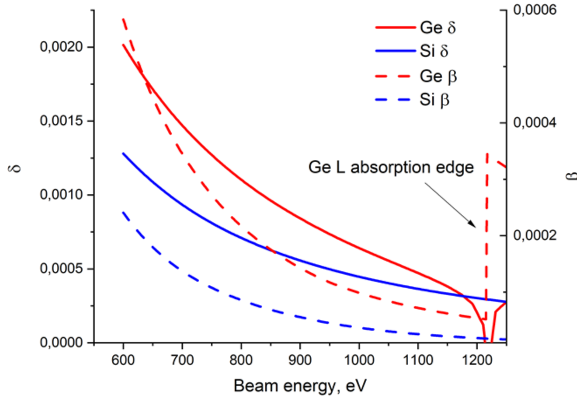

Fig. 4. Optical constants of Si and Ge in the accessible energy range.

The first set of measurements was therefore performed at 800 eV to find a compromise between the highest achievable refraction contrast, low absorption of Si and Ge and optimal operational conditions at the beamline. The second set was performed at 1230 eV, near the Ge L absorption edge, but low scattering at this energy led to very low contrast and SNR in the reconstructed images. The results of the second set of measurements can be found in Supplement 1.

Ptychographic imaging of the SiGe staircase tip at 800 eV

In this paragraph we discuss the experimental conditions, data processing routines and the results of ptychographic imaging of the SiGe staircase tip at 800 eV.

During this experiment beam energy was set to 800 eV, scan area 3 × 3 µm, beam focus spot 1 µm, scan step 60 nm (50 × 50 scan positions in rectangular grid), and the exposure time for each scan position was 200 ms. Number of counts in a single diffraction pattern was roughly $2 \cdot 10^6$, which translates into 10^7 photons per second at the detector plane.

The reconstructed images: sample's absorption (see Fig. 5(a)), phase retardance (Fig. 5(b)), and derived from them scattering quotient map (Fig. 5(c)) corresponds well to the reference SEM image (Fig. 5(d)). It is worth mentioning though that all SEM images were made at 52° angle with respect to the specimen axis due to hardware limitations, while the CDI was done at normal incidence.

To identify chemical composition of the structures present in the tip, the exact values of the peaks' coordinates in the histogram of scattering quotient map were determined (see Fig. 6(a)). To do so, we fitted the histogram with three Gaussian distributions (see Fig. 6(b)) according to equation (1) in the Methods section. Fitting coefficients are available in Table 1. Each coefficient has a distinct meaning: a – the height of the gaussian, which is proportional to the abundance of the composite, b – the peak coordinate, allows for the identification of the composite by comparing with tabular values, and c – the width of the distribution, characterizes signal-to-noise ratio, and/or presence of contaminants. The Pt material was deposited by ion beam, creating a Pt

Optics EXPRESS

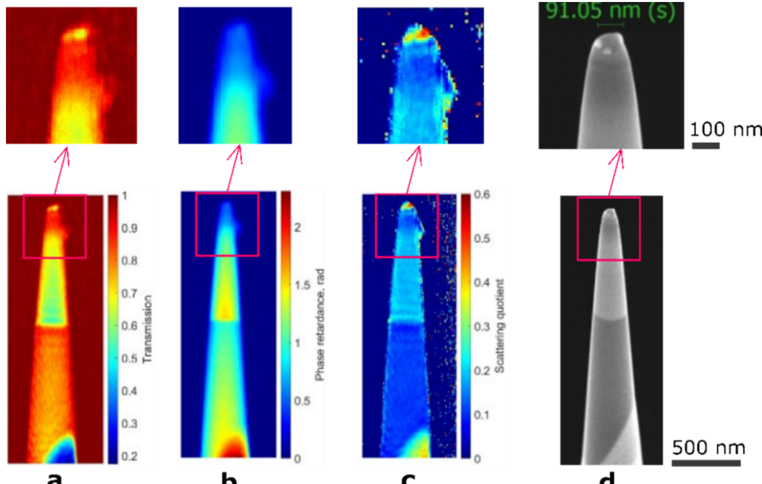

Fig. 5. SiGe staircase APT tip ptychographic imaging at 800 eV: reconstructed object transmission (a), phase retardance (b), calculated scattering quotient map (c), and SEM image (d) for comparison.

layer with considerable C contamination [58], which results in a very broad peak corresponding to a non-uniform mix of two elements.

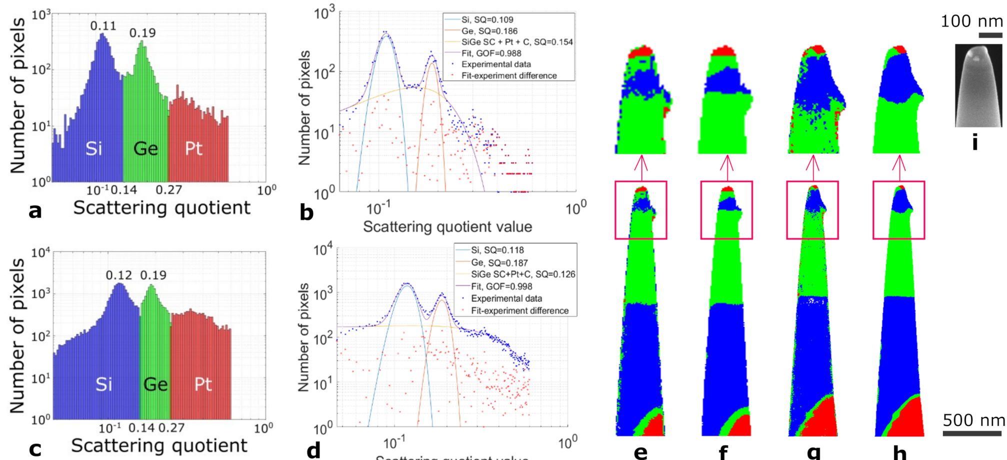

Fig. 6. Resolving chemical composites in ptychographic reconstruction of SiGe staircase APT tip: histograms of the scattering quotient maps (Fig. 5(c)) in cases of normal sampling (a) and double upsampling (c), corresponding gaussian fits (b) and (d), and resulting chemically resolved images before (e),(g) and after (f),(h) filtration; SEM image (i) included for comparison.

Table 1. Fitting parameters (see Eq. (1)) for the scattering quotient histogram shown in Fig. 6(b),(d)

a_1	b_1	c_1	a_2	b_2	c_2	a_3	b_3	c_3
248	0.11	0.0241	122	0.19	0.0348	31.8	0.15	0.250

By ranging the scattering quotient values and attributing them to a particular element using a color code (see Fig. 6(a)), the scattering quotient map (Fig. 5(c)) can be transformed into a chemically resolved image (see Fig. 6(e)) where all the composites are represented with the maximum clarity and sharper edges. Using the additional filtration procedure described in Section 5.4, we remove residual noise and small reconstruction artifacts (see Fig. 6(f)). The larger artifacts remain. For example, at the bottom of the reconstructed image there is a fake Ge layer between Pt and Si. This is the result of Pt/Si interface being not parallel to optical axis leading to its blurring. As a result, the scattering quotient values gradually transition from high values corresponding to Pt to low values corresponding to Si, which will be falsely assigned to Ge in that region. The approximation of a plane object, commonly used in ptychography, will result in blurring of any interface oriented not parallel to the optical axis with the amount of blurring proportional to the angle. In order to image 3D objects with a complex inner structure, a tomographic multi-angle approach [24] or multi-slice ptychography [59] can be used, but both require much more data acquisition, as well as processing.

Experimentally determined coordinates of Si and Ge peaks (b_1 and b_2 values in Table 1) are in a good agreement with the values of scattering quotient calculated from tabular values ($f_q = f_1/f_2$) [60,61] presented in Table 2 (see equation (3) in Section 5.3), thus confirming the validity of chemical sensitivity of the reconstruction.

Table 2. Tabular values of real f_1, imaginary f_2 parts of atomic scattering factor [60,61], corresponding scattering quotient f_q for Pt, Ge, Si and C at 800 eV, and experimentally obtained values f_{q_exp}

Material	f_1	f_2	f_q	f_{q_exp}
Pt	48.6	22.8	0.47	-
Ge	23.2	4.6	0.20	0.19
Si	13.2	1.6	0.12	0.11
C	6.35	0.936	0.15	-

3.2. Resolution estimation

With the sample thickness, light scattering on inner structures and defects increases, and plane object approximation loses its validity. This increases the complexity of the reconstruction and can lead to a decrease of the resolution since not all the structures get interpreted correctly by the algorithm. On the other hand, a thin layer of material with low absorption and low refraction will produce a very weak diffraction signal, which can also be detrimental for the reconstruction. So, here we attempt to estimate the resolution impact of those effects on the example of SiGe staircase APT tip.

Resolution test of the setup

The resolution of the experimental setup was tested with a Siemens star measurement standard as the test object. The aim of this experiment was to assess the achievable resolution of the setup at present experimental conditions. The beam energy was set to 750 eV, scan area 3×3 µm, beam focus spot 1 µm, scan step 60 nm (50×50 scan positions in total), exposure time for each scan position was 100 ms. An example of a diffraction pattern from a Siemens star (in logarithmic scale) is shown in the left of Fig. 3.

Eight iterations of the mPIE algorithm [55] were already enough to reach stagnation of the reconstruction error. Results of the reconstruction are shown in Fig. 7: reconstructed image with

Optics EXPRESS

magnified fragment in Fig. 7(a,b), reconstructed probe in Fig. 7(c), and the dependency of the reconstruction error on the number of iterations.

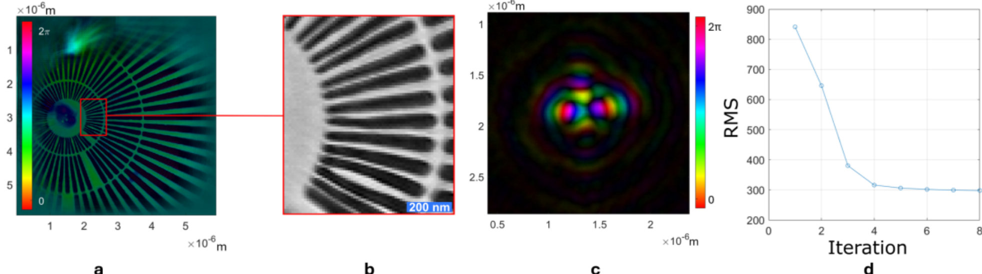

Fig. 7. The results of the reconstruction: reconstructed image (a), magnified fragment (b), reconstructed probe (c), and dependency of reconstruction error on number of iterations (d). Images (a) and (c) show complex light distributions: intensity as brightness and phase as color.

To assess the resolution in the reconstructed image we have calculated Fourier ring correlation as described in [62] using open-source software [63]. The calculated value is 12.8 nm which is very close to the pixel size of 12.2 nm.

Resolution estimation for 3D samples

In order to estimate the resolution in the ptychographically reconstructed images of the APT tip, we analyzed two sharp interfaces: Pt/Si at the apex of the tip, and Si/Ge 1.2 µm below the apex (see Fig. 1). The sample thickness at the Pt/Si interface is ∼130 nm, while at the Ge/Si it is ∼350 nm.

We measured the widths of the transition region between both materials over which the scattering quotient value (see Fig. 8(c)) changes from 90% to 10%. To measure the distance with subpixel resolution, sampling was increased by a factor of ten. Along each line (4 in case of Pt/Si and 11 for Ge/Si, see Fig. 8) the width of the transition region was measured, and the mean and standard deviation calculated. In the graphs ripples are visible around the interface which often occur near sharp interfaces or edges in CDI reconstructions. The results of the measurement are: (2.4 ± 0.2) pixels or (27 ± 2) nm for Pt/Si and (4.8 ± 0.6) pixels or (55 ± 7) nm for Ge/Si.

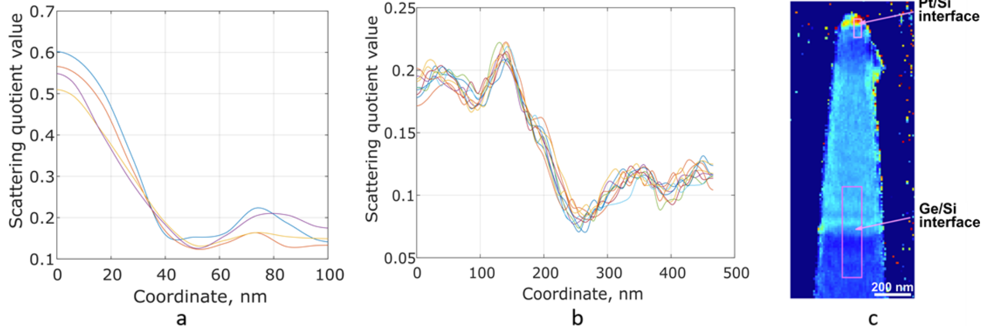

Fig. 8. Scattering quotient values along vertical lines of fragments (depicted by pink rectangles) of ptychographically reconstructed APT tip image (c) containing: Pt/Si (a) and Ge/Si (b) interfaces.

This hints that the resolution changes as function of the depth, i.e. the thickness of the sample, since the second interface corresponds to almost three times larger sample thickness. In addition,

Optics EXPRESS

difference in contrast may also affect the resolution to a certain extent. The loss in resolution with increasing sample thickness may be because the thin sample approximation is less valid, and that the sample should be better considered as a 3D rather than a 2D object when light propagation is calculated. While this is possible [24,59], that route requires more complex and extensive experiment with extra hardware capabilities, which we didn't have, plus much more extensive data processing. This kind of experiment might be the next step but goes beyond the scope of this initial work.

Another possible reason for a lower resolution at the Ge/Si interface could be an angular misalignment of the interface such that the beam does not hit the interface parallel. The relationship between the sample thickness and the resolution warrants a more thorough investigation which is outside the scope of this study.

Higher sampling in reconstructed images

Although the spatial resolution in the ptychographic reconstruction is physically limited by the wavelength of the light and the detector NA, sampling, i.e. the pixel size, can be improved by artificially increasing the size of the diffraction patterns via zero padding, thus virtually "increasing" the detection NA. While these new areas will not add any new information or help in resolving smaller features, this approach might reduce sampling artifacts, e.g. when pixel sized features end up in between two pixels. Such approach was already implemented in many works on ptychography, for example [64–66], so here we evaluate its efficiency in our case of isolated 3D nanoobjects such as APT tips.

We show below that this smoothens edges and results in less "pixelated" images, albeit at a certain cost. Firstly, it significantly increases the time for reconstruction due to much larger arrays' sizes. Secondly, the addition of large areas with no signal will decrease the overall SNR leading to a higher noise level in the reconstructed images.

The example of such "upsampled" reconstruction is shown in Fig. 6(c,d,g,h). The diffraction patterns were zero padded to twice of the original size, decreasing pixel size in the reconstruction from 11.4 nm down to 5.7 nm. This led to much smoother edges of the APT tip, which is especially noticeable in case of small features such as the tip's apex.

The histogram shown in Fig. 6(c) was fitted with three gaussian distributions (see Eq. (1)), the coefficients are presented in Table 3, the fit is shown in Fig. 6(d)

Table 3. Fitting parameters (see Eq. (1)) for the scattering quotient histograms shown in Fig. 6(d)

a_1	b_1	c_1	a_2	b_2	c_2	a_3	b_3	c_3
1410	0.118	0.0177	672	0.187	0.0204	181	0.126	0.310

The comparison between the native sampling, upsampled reconstruction, and SEM reference image, presented in Fig. 6, demonstrates beneficial effect of higher sampling for resolving of tip's apex.

Quantitative chemical imaging

As shown in Fig. 5, there is a SiGe staircase region near the apex of the tip where the ratio of Si to Ge gradually decreases. A scattering quotient map, obtained as a result of ptychographic reconstruction, allows us not only to differentiate between various chemical elements as shown in Fig. 4, but also to quantitatively measure $Si_{1-x}Ge_x$ ratio in the staircase region of the tip.

Figure 9(a) shows an enlarged fragment of the scattering quotient map of the SiGe staircase tip from Fig. 5(c). The pixels size is 11.4 nm. The plot in Fig. 9(b) below represents the scattering quotient averaged over different rows in the area depicted by a red rectangle. The error bars are the standard deviation values over rows. The horizontal red, green and blue lines indicate tabular

values of the scattering quotient [60,61]. Vertical dotted lines separate different regions of the sample and help guide the eye. The $Si_{1-x}Ge_x$ region shows very good linear dependency of the scattering quotient with the coordinates along the vertical axis (Fig. 9(d)) which corresponds well to the APT data shown in Fig. 9(e). The $Si_{1-x}Ge_x$ concentration (Fig. 9(c)) was calculated as:$(SQ(y) - SQ_{Si})/(SQ_{Ge} - SQ_{Si})$ where SQ is the scattering quotient value of the corresponding element, and y is the coordinate. Average value of standard deviation of concertation in Fig. 9(c) is 0.1, while the maximum is 0.16. The size of SiGe staircase region in the ptychographic reconstruction is 16 pixels which equals 182 nm, in agreement with the APT data.

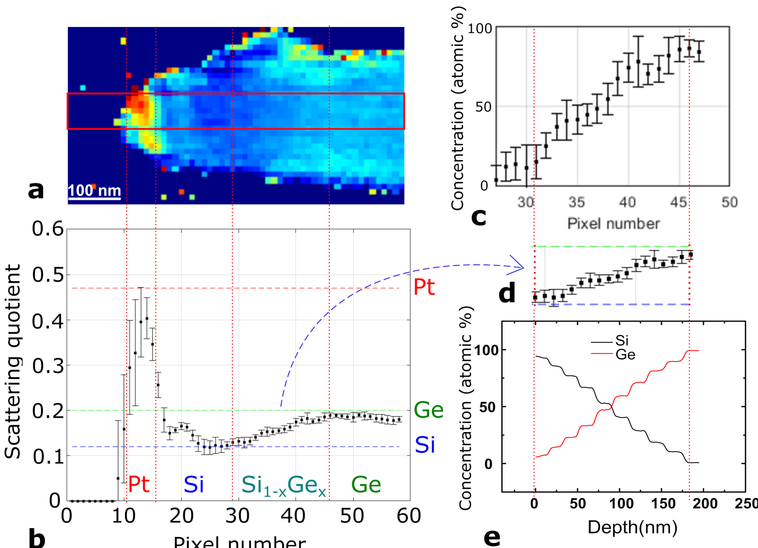

Fig. 9. Quantitative chemically resolved ptychographic imaging of the SiGe staircase: the enlarged fragment of the scattering quotient map of the SiGe staircase tip from Fig. 5(c) (a), scattering quotient value averaged over columns in the area depicted by red rectangle vs column number (b) and its enlarged fragment corresponding to the staircase region (d) calculates from scattering quotient $Si_{1-x}Ge_x$ concentration (c), and reference APT data (e).

In the top region of the tip, the transition area between the Pt cap and the Si layer is ~80 nm thick shows a scattering quotient slightly higher than the tabular value for Si or the region beneath. This could indicate some intermixing, contamination, or a non-horizontal or non-planarity of Si/Pt interface.

3.3. Assessment of geometry of low-contrast features

Our second reference system was an APT tip that contained a Si fin embedded in SiO_2 [42]. In this experiment we demonstrate the capability of ptychographic CDI to image low-contrast, nanometer sized features with high fidelity. The absorption of Si and SiO_2 at 800 eV differs by only 10%, resulting in a very low amplitude contrast (Fig. 10(a)) and negligible phase contrast (Fig. 10(b)). During this experiment the beam energy was set to 800 eV, with a scan area of 1.2×1.2 μm, a beam focus spot size of 1 μm, a 40 nm scan step (30×30 scan positions in a rectangular grid), with an exposure time for each scan position of 2 s.

SEM image of the needle (Fig. 10(h)), corresponds well to the ptychographic reconstruction (Fig. 10(c,f,g)). The smallest feature resides at the top of Si fin which is 80 nm wide. The geometry of the sample measured in ptychographically reconstructed chemically resolved images are in a good agreement with the SEM measurements (Table 4). Peak values of the scattering

Optics EXPRESS

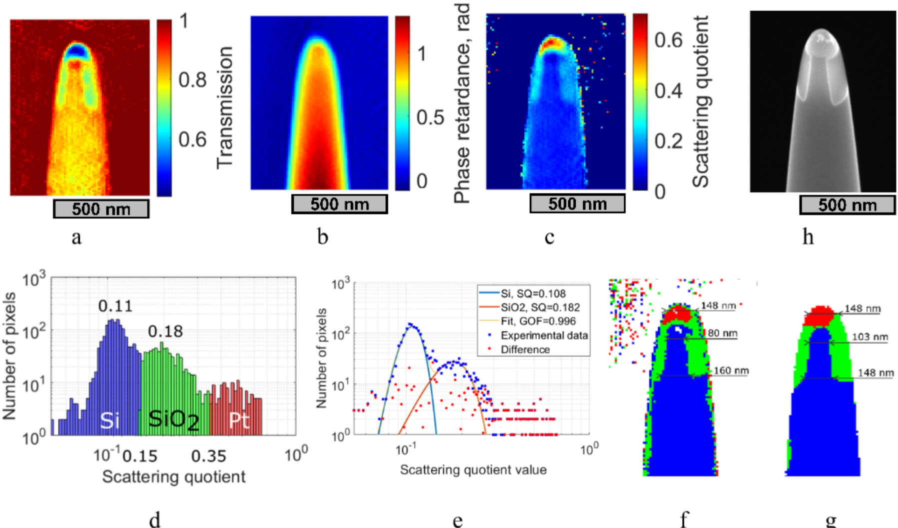

Fig. 10. Ptychographic reconstruction of the APT tip with Si fin embedded in SiO_2: reconstructed object transmission (a), phase retardance (b), calculated scattering quotient map (c), its histogram (d) and gaussian fit (e), and chemically resolved images without (f) and with (g) filtration; reference SEM image (h).

quotient for Si and SiO_2 are 0.11 and 0.18 respectively, and in good accordance with tabular values, 0.12 and 0.20, respectively.

Table 4. Comparison of the dimensions extracted from SEM and ptychography as shown in Fig. 11.

	Pt cap size, nm	Si fin size at the top, nm	Si fin size at the bottom, nm
SEM	142	79	155
Ptychography: without (with) filtration	148 (148)	80 (103)	160 (148)

Despite the low contrast of the Si fin in transmission measurements (Fig. 10(c)) and no visible contrast in the phase image (Fig. 10(b)), we achieved a chemically resolved image of the APT needle with the Si fin (Fig. 10(c,f,g)) of good quality and in excellent agreement with the geometry extracted from the SEM reference image (Table 4).

4. Conclusions

We report on the first-time soft X-ray ptychographic imaging of atom probe needles using the MAXYMUS scanning X-ray microscope at the electron storage ring BESSY II. These measurements prove that one can reconstruct the overall shape of an APT tip with a pixel size as small as 11 nm, paving the way for a potential in-lab, table-top EUV based ptychographic imaging setup for such purposes.

A spatial resolution of 13 nm was demonstrated on a thin Siemens star reference target, whereas a thickness-dependent resolution was observed for buried interfaces, i.e. a spatial resolution of 30 nm and 60 nm for a 130 nm and 350 nm thick region, respectively. In the upper region of the APT tip we were able to accurately resolve the geometry of less than 100 nm sized buried structures even for materials that have comparable absorption properties and hence exhibit a low-contrast such as Si and SiO_2. Relying on the scattering quotient, we have demonstrated the

Optics EXPRESS

potential of chemically sensitive imaging and quantitative compositional analysis by resolving the Si and Ge ratio in a thin $Si_{1-x}Ge_x$ gradient layer.

Comparing (ptychographic) CDI to other methods for the purpose of APT tip imaging, its strength would be the capability to visualize a large field of view of the needle as well as embedded nanostructures with a chemical sensitivity, without the need for specific sample preparation or the risk of possible carbon contamination build-up as could be an issue for Transmission Electron Microscopy (TEM) inspection. While in this study we have presented 2D images acquired in transmission mode, with CDI tomography one can in principle obtain 3D information, similar as to scanning probe-based methods such as Atomic Force Microscopy (AFM) [67]. At present, CDI does not exceed the spatial resolution achieved by TEM nor AFM. Yet, the possibility to perform CDI imaging with the same EUV light source as used to trigger field-evaporation during atom probe analysis [45] seems particularly promising for that imaging scheme. The feasibility of such an approach still needs to be experimentally validated, however.

5. Methods

Here we discuss the methods used in the reconstructions.

5.1. PtyLab and momentum-accelerated PIE (mPIE)

Reconstructions were performed with a PtyLab [56] opensource software available in Matlab, Python and Julia [68]. PtyLab incorporates multiple reconstruction algorithms.

In this work we used momentum-accelerated ptychographic iterative engine (mPIE) [58] algorithm which provides much faster convergence in comparison to other ptychographic algorithms [58]. mPIE is a modification of a popular extended ptychographic iterative engine (ePIE) [6]. It incorporates an idea of "momentum": when a certain value of an array element keeps changing from one iteration to another in the same direction, it gains momentum. So, when at another iteration it should change in the opposite direction, such a change is penalized, while momentum decreases. This addition to ePIE helps to avoid stagnation at local minima and speeds up the convergence rate.

The main parameters of an mPIE algorithm were chosen as follows. Gradient step sizes for both object and probe were varied in range to 0.25-1 between reconstructions, the number of probe states varied from 4 to 25, total variation regularization was set to 10^{-8}, the feedback parameter β was set to 0.3 and friction parameter η to 0.5.

5.2. Averaging over reconstructions and Gaussian fitting

Ptychographic reconstructions always contain noise and reconstruction artefacts. Since each reconstruction attempt is based on some initial random guess, each reconstruction is unique, and reconstruction noise is mostly uncorrelated between different reconstructions of the same dataset. Because of this, it is possible to reduce this noise by averaging the results of different reconstructions. Moreover, the noise distribution is also different between the different iterations of the same reconstruction, but of course much more correlated compared to different reconstructions.

We show how averaging affects quality of ptychographic reconstruction on the example of SiGe staircase tip. Detailed results on resolving inner structure and chemical composition are given in Section 3.2.

Results of averaging, along with histograms in logarithmic scale, are shown in Fig. S2 in Supplement 1.

Using MATLAB, we fitted histograms with superposition of three gaussian distributions:

$$f(x) = a_1 \exp\left(-\left(\frac{x-b_1}{c_1}\right)^2\right) + a_2 \exp\left(-\left(\frac{x-b_2}{c_2}\right)^2\right) + a_3 \exp\left(-\left(\frac{x-b_3}{c_3}\right)^2\right) \quad (1)$$

The first term represents Si peak in the histograms, the second – Ge, and the third covers all the rest: Pt, C contamination, SiGe staircase and noise. The goodness of the fit (R^2 value) in all three cases was over 0.99. Parameters of the fittings are given in Table S2 in Supplement 1. The main parameters here are b_1 and b_2 – coordinates of centers of the Si and Ge peaks. These allow us to perform chemical identification of the elements (see following section). The widths of the peaks are determined by c_1 and c_2 parameters – standard deviations (STD) of the distributions, and they are primarily affected by noise level in the reconstructions. We can see that averaging over 9 iterations leads to 11% average improvement (10% deterioration for the Si peak, and 21% improvement for the Ge peak) in STD, while averaging over 4 reconstructions – to 53% improvement (44% improvement for the Si peak, and 60% for the Ge peak).

Thus, averaging can be an effective way to increase signal-to-noise ratio at the cost of additional calculation time.

5.3. Chemically resolved imaging

Since CDI techniques enable the reconstruction of not only the amplitude distribution of the light passed through the sample but also of its phase, it is possible to identify different composites inside the sample. The attenuation (amplitude) of the light via its passage through the sample is linked to the extinction coefficient, while the magnitude of the phase shift is dependent on the refraction coefficient. Obviously, attenuation and phase shift also depend on the thickness of the sample at any given point, so without knowing it, it is not possible to extract actual values of the coefficients. However, there is a parameter which can be calculated based on the attenuation and phase shift only: scattering quotient [7]. It is independent of thickness and can be calculated as:

$$f_q = \frac{\ln(|T|)}{\varphi}, \tag{2}$$

where |T| - is a matrix of magnitude values of a complex transmission function of the reconstructed object, and φ – is a matrix of its phase retardation values.

At the same time, scattering quotient can be calculated as:

$$f_q = \frac{\overline{f_2}}{\overline{f_1}}, \tag{3}$$

where $\overline{f_1}$ and $\overline{f_2}$ are the average (along the optical path) values of real and imaginary parts of the complex atomic scattering factor $\tilde{f} = f_1 + if_2$. The real part of it characterizes refractive properties of atoms, while the imaginary one describes the absorption. These values can be found in CXRO [63] or NIST [64] databases for most chemical elements.

5.4. Chemically resolved images filtration procedure

For removal of reconstruction artifacts, we developed and implemented additional filtration procedure. We will show how it works using reconstruction shown in Fig. 5 as an example. First, we obtain "chemical density" maps based on chemically resolved image, like the one shown in Fig. 6(e). For each image pixel we calculated the amount of every element in a certain radius r_c (in this case it was 5 pixels). Then, each pixel is assigned value corresponding to the highest density in the neighborhood but only if it belongs to the sample (not background) and density is above certain threshold (20% in this case).

This step removes small (several pixel across) inclusions of different elements into homogeneous areas. After that, all pixels with chemical density above second threshold (40%) are assigned with highest density element value. This helps to remove background inclusions from inside the sample image.

Optics EXPRESS

Ptychography reconstructions often suffer from ringing artifacts in areas of rapid change of phase and/or amplitude. You can see them on the edges of the sample in Fig. 5(c). To get rid of those we checked the chemical composition image against transmission and phase of the reconstructed images (see Fig. 5(a,b)): if either transmissivity was above certain level t_t (0.96) or phase retardance below certain threshold t_p (0.15 rad), image pixel was assigned the background value. Processed in this way, the final chemically resolved image is presented in Fig. 6(f). All the reconstruction artifacts were successfully removed except for the false Ge stripe at the bottom of the image due to its sufficiently large dimensions (4 pixels ~50 nm). The probable reason for its appearance is lower resolution due to the higher sample thickness in that region (~600 nm) and non-planar shape of the interface.

Funding. Fonds Wetenschappelijk Onderzoek (AKUL 15-22 ZKD 1037).

Acknowledgments. We thank Dr. Markus Weigand for the technical support of the experiment and all people involved in the construction and operation of the MAXYMUS scanning X-ray microscope at HZB, BESSY II in Berlin.

Disclosures. The authors declare no conflicts of interest.

Data availability. Data underlying the results presented in this paper are not publicly available at this time but may be obtained from the authors upon reasonable request.

Supplemental document. See Supplement 1 for supporting content.

References

1. O. Bunk, M. Dierolf, S. Kynde, *et al.*, "Influence of the overlap parameter on the convergence of the ptychographical iterative engine," Ultramicroscopy **108**(5), 481–487 (2008).
2. G. Varnavides, S. M. Ribet, S. E. Zeltmann, *et al.*, "Iterative Phase Retrieval Algorithms for Scanning Transmission Electron Microscopy," (2023).
3. J. R. Fienup, "Phase retrieval algorithms: a comparison," Appl. Opt. **21**(15), 2758–2769 (1982).
4. D. R. Luke, "Relaxed averaged alternating reflections for diffraction imaging," Inverse Probl. **21**(1), 37–50 (2005).
5. J. M. Rodenburg and H. M. L. Faulkner, "A phase retrieval algorithm for shifting illumination," Appl. Phys. Lett. **85**(20), 4795–4797 (2004).
6. A. M. Maiden and J. M. Rodenburg, "An improved ptychographical phase retrieval algorithm for diffractive imaging," Ultramicroscopy **109**(10), 1256–1262 (2009).
7. M. W. M. Jones, K. Elgass, M. D. Junker, *et al.*, "Mapping biological composition through quantitative phase and absorption X-ray ptychography," Sci. Rep. **4**(1), 6796 (2014).
8. P. D. Baksh, M. Ostrčil, M. Miszczak, *et al.*, "Quantitative and correlative extreme ultraviolet coherent imaging of mouse hippocampal neurons at high resolution," Sci. Adv. **6**(18), 1 (2020).
9. M. Dierolf, A. Menzel, P. Thibault, *et al.*, "Ptychographic X-ray computed tomography at the nanoscale," Nature **467**(7314), 436–439 (2010).
10. D. F. Gardner, H. C. Kapteyn, M. D. Seaberg, *et al.*, "Full field tabletop EUV coherent diffractive imaging in a transmission geometry," Opt. Express **21**(19), 21970–21980 (2013).
11. D. F. Gardner, H. C. Kapteyn, M. D. Seaberg, *et al.*, "Tabletop nanometer extreme ultraviolet imaging in an extended reflection mode using coherent Fresnel ptychography," Optica **1**(1), 39–44 (2014).
12. B. Zhang, D. F. Gardner, M. D. Seaberg, *et al.*, "High contrast 3D imaging of surfaces near the wavelength limit using tabletop EUV ptychography," Ultramicroscopy **158**, 98–104 (2015).
13. Y. Esashi, N. W. Jenkins, Y. Shao, *et al.*, "Tabletop extreme ultraviolet reflectometer for quantitative nanoscale reflectometry, scatterometry, and imaging," Rev. Sci. Instrum. **94**(12), 123705 (2023).
14. J. Vila-Comamala, A. Diaz, M. Guizar-Sicairos, *et al.*, "Characterization of high-resolution diffractive X-ray optics by ptychographic coherent diffractive imaging," Opt. Express **19**(22), 21333–21344 (2011).
15. T. A. Butcher, N. W. Phillips, C. C. Chiu, *et al.*, "Ptychographic Nanoscale Imaging of the Magnetoelectric Coupling in Freestanding BiFeO3," Adv. Mater. **36**(23), 2311157 (2024).
16. R. L. Sandberg, A. Paul, D. A. Raymondson, *et al.*, "Lensless diffractive imaging using tabletop coherent high-harmonic soft-X-ray beams," Phys. Rev. Lett. **99**(9), 098103 (2007).
17. P. Helfenstein, I. Mohacsi, R. Rajeev, *et al.*, "Scanning coherent diffractive imaging methods for actinic extreme ultraviolet mask metrology," J. Micro/Nanolith. MEMS MOEMS **15**(3), 034006 (2016).
18. I. Mochi, P. Helfenstein, R. Rajeev, *et al.*, "Actinic inspection of EUV reticles with arbitrary pattern design," Proc. SPIE **10450**, 1045007 (2017).
19. H.-S. Kim, U. Locans, R. M. Nebling, *et al.*, "High resolution and uniform image reconstruction in a large field-of-view for EUV actinic mask review," Proc. SPIE **11518**, 115180X (2020).
20. P. Ansuinelli, B. Bejar, Y. Ekinci, *et al.*, "Towards fast ptychography image reconstruction of EUV masks by deep neural networks," in (SPIE-Intl Soc Optical Eng, 2023), p. 44.

21. E. R. Shanblatt, C. L. Porter, D. F. Gardner, *et al.*, "Quantitative Chemically Specific Coherent Diffractive Imaging of Reactions at Buried Interfaces with Few Nanometer Precision," Nano Lett. **16**(9), 5444–5450 (2016).
22. W. Eschen, L. Loetgering, V. Schuster, *et al.*, "Material-specific high-resolution table-top extreme ultraviolet microscopy," Light: Sci. Appl. **11**(1), 117 (2022).
23. M. Tanksalvala, C. L. Porter, Y. Esashi, *et al.*, "Nondestructive, high-resolution, chemically specific 3D nanostructure characterization using phase-sensitive EUV imaging reflectometry," Sci. Adv. **7**(5), 9667–9694 (2021).
24. Y. C. Karen, C. Wiegart, S. S. Kim, *et al.*, "Revealing Three-Dimensional Morphology in Nanoporous Gold Using Three-Dimensional X-Ray Fresnel Coherent Diffractive Imaging Tomography," J. Electrochem. Energy Conversion and Storage **17**(4), 041005 (2020).
25. H. Lu, M. Odstrčil, C. Pooley, *et al.*, "Characterisation of engineered defects in extreme ultraviolet mirror substrates using lab-scale extreme ultraviolet reflection ptychography," Ultramicroscopy **249**, 113720 (2023).
26. Y. H. Lo, C. T. Liao, J. Zhou, *et al.*, "Multimodal x-ray and electron microscopy of the Allende meteorite," Sci. Adv. **5**(9), 1 (2019).
27. Y. Jiang, Z. Chen, Y. Han, *et al.*, "Electron ptychography of 2D materials to deep sub-ångström resolution," Nature **559**(7714), 343–349 (2018).
28. Z. Chen, Y. Jiang, Y. T. Shao, *et al.*, "Electron ptychography achieves atomic-resolution limits set by lattice vibrations," Science **372**(6544), 826–831 (2021).
29. X. Pei, L. Zhou, C. Huang, *et al.*, "Cryogenic electron ptychographic single particle analysis with wide bandwidth information transfer," Nat. Commun. **14**(1), 3027 (2023).
30. P. van der Heide, I. Mathotkin, W. Vandervorst, *et al.*, "APT Tip Shape Modifications During Analysis, Its Implications, and the Potential to Measure Tip Shapes in Real Time via Soft-X-Ray Ptychography," Microscopy Microanal. **25**(S2), 2504–2505 (2019).
31. B. Gault, A. Chiaramonti, O. Cojocaru-Mirédin, *et al.*, "Atom probe tomography," Nat. Rev. Methods Primers **1**(1), 51 (2021).
32. A. D. Giddings, S. Koelling, Y. Shimizu, *et al.*, "Industrial application of atom probe tomography to semiconductor devices," Scr. Mater. **148**, 82–90 (2018).
33. P. Bas, A. Bostel, B. Deconihout, *et al.*, "A general protocol for the reconstruction of 3D atom probe data," Appl. Surf. Sci. **87-88**(C), 298–304 (1995).
34. B. P. Geiser, D. J. Larson, E. Oltman, *et al.*, "Wide-Field-of-View Atom Probe Reconstruction," Microscopy Microanal. **15**(S2), 292–293 (2009).
35. F. Vurpillot, D. Larson, and A. Cerezo, "Improvement of multilayer analyses with a three-dimensional atom probe," Surface Interface Anal. **36**(5-6), 552–558 (2004).
36. F. Vurpillot, M. Gruber, G. Da Costa, *et al.*, "Pragmatic reconstruction methods in atom probe tomography," Ultramicroscopy **111**(8), 1286–1294 (2011).
37. E. A. Marquis, B. P. Geiser, T. J. Prosa, *et al.*, "Evolution of tip shape during field evaporation of complex multilayer structures," J. Microsc. **241**(3), 225–233 (2011).
38. A. Grenier, S. Duguay, J. P. Barnes, *et al.*, "3D analysis of advanced nano-devices using electron and atom probe tomography," Ultramicroscopy **136**, 185–192 (2014).
39. D. Melkonyan, C. Fleischmann, L. Arnoldi, *et al.*, "Atom probe tomography analysis of SiGe fins embedded in SiO2: Facts and artefacts," Ultramicroscopy **179**, 100–107 (2017).
40. J. P. Barnes, A. Grenier, I. Mouton, *et al.*, "Atom probe tomography for advanced nanoelectronic devices: Current status and perspectives," Scr. Mater. **148**, 91–97 (2018).
41. J. Op De Beeck, J. E. Scheerder, B. P. Geiser, *et al.*, "The Prospect of Spatially Accurate Reconstructed Atom Probe Data Using Experimental Emitter Shapes," Microscopy Microanal. **28**(4), 1141–1149 (2022).
42. C. Fletcher, M. P. Moody, C. Fleischmann, *et al.*, "Automated calibration of model-driven reconstructions in atom probe tomography," J. Phys. D. Appl. Phys. **55**(37), 375301 (2022).
43. D. Haley, T. Petersen, S. P. Ringer, *et al.*, "Atom probe trajectory mapping using experimental tip shape measurements," J. Microsc. **244**(2), 170–180 (2011).
44. "Extending continuum models for atom probe simulation - ORA - Oxford University Research Archive," https://ora.ox.ac.uk/objects/uuid:04c9cc81-89f6-4399-9242-1cef7739238a.
45. B. W. Caplins, A. N. Chiaramonti, J. M. Garcia, *et al.*, "Atom probe tomography using an extreme ultraviolet trigger pulse," Rev. Sci. Instruments **94**(9), 93704 (2023).
46. J. Mayer, J. Barthel, A. Vayyala, *et al.*, "The TOMO Project – Integrating a Fully Functional Atom Probe in an Aberration-Corrected TEM," Microscopy Microanal. **29**(Supplement_1), 593–594 (2023).
47. H. Jiang, C. Song, C. C. Chen, *et al.*, "Quantitative 3D imaging of whole, unstained cells by using X-ray diffraction microscopy," Proc. Natl. Acad. Sci. U S A **107**(25), 11234–11239 (2010).
48. T. Kimura, Y. Joti, A. Shibuya, *et al.*, "Imaging live cell in micro-liquid enclosure by X-ray laser diffraction," Nat. Commun. **5**(1), 3052 (2014).
49. T. McJunkin, B. Harpt, Y. Feng, *et al.*, "SiGe quantum wells with oscillating Ge concentrations for quantum dot qubits," Nat. Commun. **13**(1), 7777 (2022).
50. G. Scappucci, P. J. Taylor, J. R. Williams, *et al.*, "Crystalline materials for quantum computing: Semiconductor heterostructures and topological insulators exemplars," MRS Bulletin **46**(7), 596–606 (2021).

Optics EXPRESS

51. S. Lee, H. Kim, S. T. Lee, *et al.*, "SiO2Fin-Based Flash Synaptic Cells in and Array Architecture for Binary Neural Networks," IEEE Electron Device Lett. **43**(1), 142–145 (2022).
52. S. Panchanan, R. Maity, A. Baidya, *et al.*, "Role of Fin Shape on Drain Current of SiO2/HfO2 Based Trigate FinFET Including Quantum Mechanical Effect," Silicon **15**(9), 3883–3895 (2023).
53. I. Bykova, "High-resolution X-ray ptychography for magnetic imaging," PhD dissertation, Max-Planck-Institut für Intelligente Systeme (2018).
54. P. S. Jørgensen, L. Besley, A. M. Slyamov, *et al.*, "Hard x-ray grazing-incidence ptychography: large field-of-view nanostructure imaging with ultra-high surface sensitivity," Optica **11**(2), 197–204 (2024).
55. D. Johnson, P. Li, and A. Maiden, "Further improvements to the ptychographical iterative engine," Optica **4**(7), 736–745 (2017).
56. L. Loetgering, M. Du, D. B. Flaes, *et al.*, "PtyLab.m/py/jl: a cross-platform, open-source inverse modeling toolbox for conventional and Fourier ptychography," (2023).
57. M. K. Miller, K. F. Russell, K. Thompson, *et al.*, "Review of Atom Probe FIB-Based Specimen Preparation Methods," Microscopy Microanal. **13**(6), 428–436 (2007).
58. N. T. H. Farr, G. M. Hughes, and C. Rodenburg, "Monitoring carbon in electron and ion beam deposition within fib-sem," Materials **14**(11), 3034 (2021).
59. J. Lee, M. Lee, Y. Park, *et al.*, "Multislice Electron Tomography Using Four-Dimensional Scanning Transmission Electron Microscopy," Phys. Rev. Appl. **19**(5), 054062 (2023).
60. "CXRO X-Ray Interactions With Matter," (n.d.).
61. "X-Ray Transition Energies Database | NIST," (n.d.).
62. B. Rieger, B. Rieger, I. Droste, *et al.*, "Single image Fourier ring correlation," Opt. Express **32**(12), 21767–21782 (2024).
63. B. Rieger and S. Stallinga, "1FRC," https://gitlab.tudelft.nl/imphys/ci/1frc.
64. J. M. Rodenburg, F. Zhang, F. Berenguer, *et al.*, "Translation position determination in ptychographic coherent diffraction imaging," Opt. Express **21**(11), 13592–13606 (2013).
65. H. Sha, J. Cui, J. Li, *et al.*, "Ptychographic measurements of varying size and shape along zeolite channels," Sci. Adv. **9**(11), 1 (2023).
66. J. Cui, H. Sha, W. Yang, *et al.*, "Antiferromagnetic imaging via ptychographic phase retrieval," Sci. Bull. **69**(4), 466–472 (2024).
67. F. Ohnesorge and G. Binnig, "True Atomic Resolution by Atomic Force Microscopy Through Repulsive and Attractive Forces," Science **260**(5113), 1451–1456 (1993).
68. "PtyLab · GitHub," https://github.com/PtyLab.